Available online at www.sciencedirect.com

jmr&t Journal of Materials Research and Technology

journal homepage: www.elsevier.com/locate/jmrt

Piezoresistive behavior of MWCNT/PA12 honeycomb composites processed via selective laser sintering

Muhammad Umar Azam [a], *Andreas Schiffer* [a,*], *S. Kumar* [b,**]

[a] *Department of Mechanical Engineering, Khalifa University, P.O. Box 127788, Abu Dhabi, United Arab Emirates*
[b] *James Watt School of Engineering, University of Glasgow, Glasgow, G12 8QQ, UK*

ARTICLE INFO

Article history:
Received 9 May 2023
Accepted 7 August 2023
Available online 10 August 2023

Keywords:
Polymer-matrix composites (PMCs)
Honeycomb structures
Selective laser sintering (SLS)
Strain sensing
Piezoresistivity

ABSTRACT

This study examines the piezoresistive and mechanical behaviors of multiwalled carbon nanotube (MWCNT)/polyamide (PA12) lattice composites processed via selective laser sintering (SLS). Firstly, neat PA12 powder was ballmilled with either 0.3, 0.5, or 1.0 wt% MWCNT loading to obtain nanoengineered powder feedstocks. The feedstocks were used to realize electrically conductive MWCNT/PA12 bulk and honeycomb lattice structures via SLS. The piezoresistive and mechanical characteristics of bulk samples were assessed under tensile, compressive, and flexure loadings while those of honeycombs were investigated under in-plane and out-of-plane compression. The morphological and thermal characterizations were carried out to gain insight into the processing-structure-property relations. The microstructural observations, including *in situ* μ-CT imaging, revealed that the porosity of the sintered parts significantly increased (≈150%) with increasing MWCNT loading, resulting in reduced elastic stiffness and strength of the sintered composites, despite their slightly higher crystallinity (+6% for 0.5 wt% MWCNT loading). The bulk nanocomposites exhibited excellent piezoresistive characteristics, showing a maximum gauge factor of 31 (in compression), which is significantly higher than the sensitivity factors of extant piezoresistive self-sensing composites. The honeycomb structures showed a maximum specific energy absorption of 3 and 24 J g^{-1} at 40% relative density under in-plane and out-of-plane compression loading, respectively. It was also demonstrated, that the MWCNT/PA12 honeycombs possess excellent strain sensing characteristics due to their pronounced piezoresistivity, reporting gauge factors up to 25 and 17 for in-plane and out-of-plane loading, respectively.

1. Introduction

The research in polymer-based multifunctional composites has rapidly advanced over the last few decades and has led to the development of material systems with complex architecture and/or composition which are beneficial for many practical applications in strain/temperature sensing [1–3], flame retardance [4], electromagnetic interference (EMI) shielding [5], tribological coatings [6], dielectrics [7], and self-healing [8],

* Corresponding author.
** Corresponding author.
E-mail addresses: andreas.schiffer@ku.ac.ae (A. Schiffer), msv.kumar@glasgow.ac.uk (S. Kumar).

https://doi.org/10.1016/j.jmrt.2023.08.051

etc. Moreover, polymer-based composites with continuous or discontinuous micro- and/or nano-scale fibers, are increasingly being used for structural applications in the automotive, aerospace, energy, defense and medical industries [9] due to their high mass-specific strength and stiffness properties, and chemical resistance [10]. However, the microstructure of such composites is typically complex which makes it challenging to produce defect-free parts with any manufacturing technique. Hence, as-manufactured polymer-based composites almost always contain multiscale flaws or defects which can grow to a critical size during in-service loading [11]. Therefore, real-time tracking of the deformation and damage state in a structure plays a vital role in detecting early signs of damage so that timely intervention can be made to guarantee the overall safety of the structural systems. Hence, there is a need to develop a system/technique capable of continuously monitoring the structural health of a component so that its service life can be enhanced, and catastrophic failure be avoided. In this context, the piezoresistive self-sensing technique, amongst others, has emerged as an enabling technology that provides a compact, efficient and cost-effective solution for real-time monitoring of the mechanical integrity of a structure, enabling early detection of damage and reducing the risk of catastrophic failure [12].

Additive manufacturing (AM), also known as 3D printing, has become a widespread technique for the fabrication of composite structures because it offers significant advantages over traditional manufacturing techniques, such as design flexibility and freedom, dimensional accuracy, low material wastage, reliability and rapid prototyping. In fact, considerable research effort is currently being devoted towards AM of composite materials to enhance their mechanical attributes and impart new functional properties. The 3D printing technology enables fabrication of a structural component with multi functionality (e.g. with the ability to self-heal or sense changes in the deformation/damage state or in the environment) in a single step without any post-processing (e.g. functional coatings etc.) as compared to conventional manufacturing processes [13]. Particularly in the context of self-sensing structures, AM has proven to be a reliable and powerful technique for creating electrically conductive polymer composites (ECPCs) with remarkable strain and damage sensing performance [1,14–16]. For example, Verma et al. [1] processed MWCNT/polypropylene nanocomposites via fused filament fabrication (FFF) technique and evaluated the thermo-piezoresistive behavior of the nanocomposites. Andrew et al. [14] evaluated the piezoresistive performance of polyetheretherketone (PEEK)-based nanocomposites processed via FFF, while Verma et al. [15] used the FFF technique to fabricate polymer-based self-sensing nanocomposites for biomedical applications. Poompiew et al. [16] developed CNT/polyurethane-based highly flexible strain sensors processed via digital light processing (DLP) technique. Recently, Hernandez et al. [17] developed the carbon nanofiber/polylactic acid composites via FFF for strain sensors. They evaluated the piezoresistive behavior of these sensors under monotonic and cyclic loadings and demonstrated stable performance.

Among various AM techniques, selective laser sintering (SLS) offers various advantages such as relatively high mechanical strength of the printed parts, recyclability of powder feedstock, and the ability to print large batches without the need for a support material [18–20]. In SLS, powder particles are selectively sintered using a laser heat source. As the first layer of powder particles is sintered, subsequent layer of powder particles are spread on the print bed through a roller and the process is continued until the final part is obtained. Despite its advantages, polymer-based SLS method has thus far only been effectively utilized for a limited class of thermoplastics due to the complex diffusional and flow processes involved in sintering of the powder feedstock [21].

Polyamide (PA12) has been extensively processed via SLS 3D printing, due to its semi-crystalline structure, appropriate average molecular weight (20–50 kDa [22]), medium range melt-viscosity (1400 Pa s at 210 °C [23]), high thermal stability and wide sintering window (20–30 °C [24]). Moreover, PA12 has good mechanical properties such as tensile strength (46 MPa), modulus (1750 MPa) and impact strength (87 kJ m^{-2}) [25], relatively low moisture absorption, high chemical stability and excellent resistance to fatigue and creep [24,26]. Caulfield et al. [27] studied the effect of various process parameters on mechanical properties of polyamide processed via SLS and found that for each parameter, there was an optimum, at which the part showed maximum mechanical properties. Schmid et al. [28] investigated the influence of origin of two commercially available PA12 powders on process parameters and properties of printed parts. Although the same grade of PA12 was used, they found differences in the properties of the 3D printed parts, due to differences in the synthesis methods of the two powders that changed their properties (e.g. crystallinity, particle size etc.). Moeskops et al. [29] studied the creep behavior of laser sintered PA12 parts and found a linear relation that can predict the creep behavior over a span of 11 years. Recently, Schneider et al. [18] fabricated PA12 3D-printed bulk and cellular structures via SLS and evaluated the constitutive parameters of the 3D printed materials.

Recent research efforts have been directed towards the fabrication of electrically conductive PA12 nanocomposites via SLS [30–32]. For example, Athreya et al. [30], fabricated laser sintered carbon black (CB)/PA12 composites with the addition of 4 wt% CB synthesized via ball milling. The 3D printed CB/PA12 were found to exhibit a five-fold increase in electrical conductivity as compared to neat PA12. However, a reduction in the mechanical properties due to segregation of CB was also reported. Yuan et al. [31] developed laser sintered electrically conductive MWCNT/PA12 and MWCNT/TPU nanocomposites and compared their thermal and electrical conductivities with their respective hot-compressed specimens. They found higher electrical conductivities for laser-sintered specimens as compared to hot-compressed ones whereas an opposite trend was observed for thermal conductivities. Recently, Xiong [32] successfully fabricated electrically conductive carbon nanotubes (CNTs) incorporated composites via SLS. However, they observed that the incorporation of CNTs in the PA12 matrix reduced the mechanical properties (tensile strength and elastic modulus) of the composites, which was attributed to the decrease in the melt flow index (MFI). Due to lower MFI, the sintering process in the composite was less effective as compared to neat PA12, resulting in higher porosity.

It is to be noted that among various conductive fillers, CNTs have exceptional electrical as well as mechanical properties.

Therefore, they are extensively being utilized as multifunctional fillers in the fabrication of polymer composites. Due to high aspect ratio of the CNTs, the conductive paths between the fillers in the polymer matrix can be established even at low percolation thresholds [33]. However, uniform dispersion of the CNTs in the polymer matrix is a major challenge to tapping their full potential.

Although a significant body of literature exists on SLS of bulk multifunctional nanocomposites [30,31,34,35], it remains unclear whether SLS technique can be effectively utilized to fabricate cellular nanocomposites exhibiting strain and damage sensing capabilities. Therefore, this study focuses on the development of MWCNT/PA12 bulk and cellular composite structures via SLS that exhibit an excellent combination of mass-specific mechanical properties (stiffness, strength and energy absorption) and the ability to self-monitor the degree of deformation or damage induced in a structure via piezoresistive sensing. To the best of our knowledge, this study is the first to examine the mechanical and piezoresistive sensing performance of MWCNT/PA12 bulk and cellular structures processed via SLS for self-sensing structural applications. Specifically, we limit our attention to hexagonal honeycomb structures due to their widespread use in an array of applications, including construction, aerospace and automotive industries [36], but it should be noted that the concept of self-sensing can also be applied to other types of structures such as 3D lattices or sandwich structures [37,38]. To enable the fabrication of such self-sensing composite structures, MWCNT/PA12 composite powders (with different wt.% MWCNTs) were first prepared via low-energy ball milling and were then used as the feedstock for 3D printing via SLS. The mechanical and piezoresistive properties of the bulk and cellular nanocomposites were experimentally evaluated and discussed in relation to their morphological and thermal characteristics. The nanocomposite honeycombs showed excellent self-sensing characteristics due to their pronounced piezoresistive behavior, both under in-plane and out-of-plane loadings.

2. Experimental procedure

2.1. Materials

Polyamide (PA12) polymer powder (particle size in the range of 35–45 μm) was obtained from BASF 3D Printing Solutions GmbH, Germany. MWCNT bundles grown by chemical vapor deposition (CVD) were provided by Applied Nanostructured Solutions LLC, USA. Further details on the MWCNTs used in this study can be found elsewhere [15,39]. It is noted that the powder feedstock was aged artificially to maintain uniform properties from first to the last print, as suggested in the literature [18]. During the aging process, the powder in the machine underwent a heating and cooling cycle in air over a temperature range of 120–25 °C.

2.2. Feedstock synthesis: preparation of nanocomposite powders

As shown in Fig. 1, nanocomposite powders were prepared by ball milling the as-received PA12 powder mixed with a predetermined amount of MWCNTs for 45 min at 150 rpm using a planetary mill (Pulverisette 5, Fritsch, Germany). The quantity of MWCNT was varied to obtain composite powders with either 0.3, 0.5 or 1.0 wt% MWCNT loading, which are henceforth referred to as PA-0.3, PA-0.5 and PA-1, respectively. Note that the speed of the ball mill (150 rpm) was chosen high enough to enable uniform dispersion of the MWCNTs in the powder, yet low enough to preserve the nearly spherical shape of the as-received PA12 powder particles (see Fig. S3, Supplementary Material). Spherical shape of the particles facilitates the flow and fusion of the powder during the sintering process [28].

2.3. 3D printing of bulk and cellular nanocomposites via SLS

A Sharebot SnowWhite printer with a CO_2 laser was used to print honeycomb structures measuring $26 \times 26 \times 17\ mm^3$ with a relative density of 40%. As shown in Fig. S7 (Supplementary Material), each honeycomb structure consisted of a 3×3 array of hexagonal unit cells with dimensions $t = 1.1$ mm, $L = 4$ mm, $H = 3.7$ mm and $\Theta = 110^{\circ}$. In addition, dogbone specimens, prismatic specimens and flexural specimens were printed to measure the bulk properties of the 3D printed nanocomposites under uniaxial tension and compression, and bending respectively, as detailed in Section 2.5. The obtained nanocomposite powders (see Section 2.2) as well as the as-received PA12 powder were used as the feedstock for all prints. The SLS process parameters were optimized executing a series of test prints for each composition and are summarized in Table S1 (Supplementary Material). It is noted that the MWCNTs present in the powder tend to absorb additional laser energy [40], enhancing the overall thermal conductivity and reducing the melting temperature T_m of the powder, as observed from the DSC thermograms (Fig. 2) which will be further discussed in Section 3.1. Hence, the powders with higher MWCNT loading were printed with lower bed temperatures (see Table S1, Supplementary Material) to avoid undesired fusion of particles in the non-laser irradiated powder bed, also referred to as hard caking (see Fig. S1, Supplementary Material).

2.4. Morphological and thermal characterization

A *scanning electron microscope* (*SEM*) (Nova NanoSEM 650, FEI) was used to characterize the morphology of the powders as well as the fracture surfaces of the printed samples. All samples were gold coated (10 nm) prior to SEM scanning to avoid charging effects.

Differential scanning calorimetry (*DSC*) (DSC131 EVO, Setaram instrumentation) was carried out to determine the melting and crystallization temperatures as well as the melting enthalpies and crystallinities of the powder samples. The analysis was performed using aluminum crucibles in the temperature range of 25–250 °C with a heating/cooling rate of 10 °C min^{-1} using N_2 as a purge gas. The crystallinity percentage (X) was calculated as follows:

$$X = \frac{\Delta H_m}{H_{100}}\ 100 \tag{1}$$

where ΔH_m is the melting enthalpy of the sample and H_{100} is the enthalpy of fusion of 100% crystalline polymer (209 J g^{-1} for PA12 [41]).

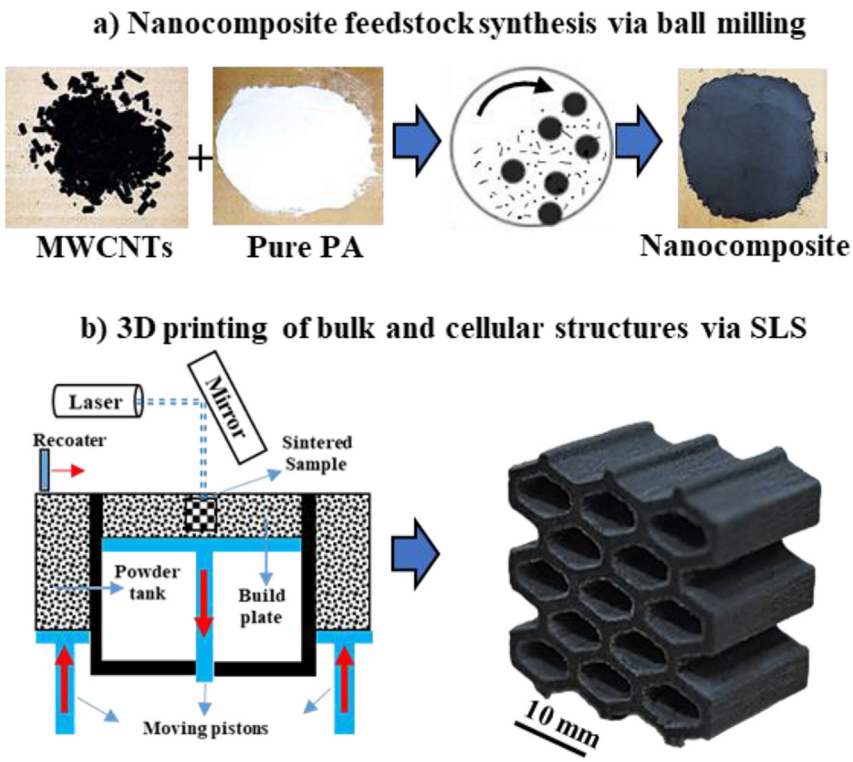

Fig. 1 – Schematic showing the manufacturing process: a) ball milling and b) additive manufacturing via selective laser sintering (SLS).

Thermogravimetric Analysis (TGA) (SDT-Q600, TA instruments) was carried out to evaluate the thermal degradation temperatures (T_d) and weight losses of the powder samples. This analysis allows determining the effect of MWCNT addition on the thermal stability of the samples and was performed using aluminum crucibles in the temperature range of 25–600 °C with a heating rate of 10 °C min^{-1}. N_2 was used as a purge gas during the experiment. Note that T_d was identified by taking the first derivative of a TGA curve and is known as derivative thermogravimetry (DTG) curve.

Micro-Computed Tomography Analysis (*μ-CT*) was carried out to evaluate the porosity in the specimens by using a Phoenix nanotom® M nanoCT 3D scanner (GE Sensing & Inspection Technologies GmbH). The specimens were scanned at a resolution of 15 μm. For the *in situ* scans, a micro compression stage with a 5 kN load sensor (Deben, UK) was used for uniaxial compression testing. The prismatic 3D printed bulk sample (width = 8 mm, depth = 8 mm, height = 12 mm) was tested at a crosshead speed of 0.5 mm min^{-1}. The loading was interrupted at 5, 10, 30 and 54% compressive strain to perform

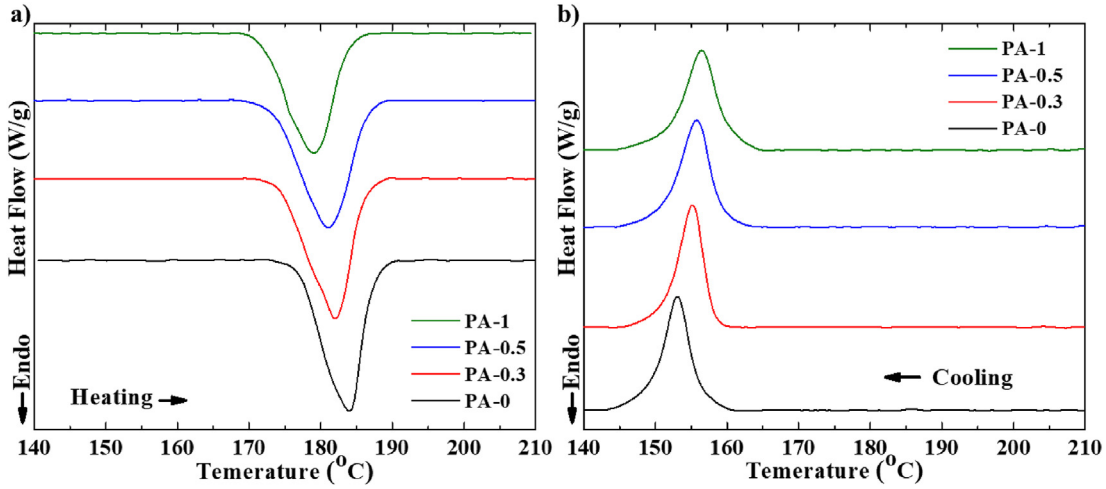

Fig. 2 – DSC thermograms of pure PA12 and MWCNT/PA12 nanocomposites for (a) heating (b) cooling cycles.

X-ray scans of the deformed specimen. Prior to performing the scans at each strain level, the specimen was allowed to relax for a time of 1 h to avoid image distortion due to possible movement of the polymeric chains as a result of their viscoelastic nature. Further details on the correlation between relaxation time and image quality of *in situ* μ-CT scans can be found in the literature [42].

2.5. Mechanical tests

Uniaxial tensile tests were performed on 3D printed dogbone specimens of 2 × 5 × 35 mm^3 gauge section (in accordance with ASTM D638 Type IV). These tests were performed using a Zwick (Z005) universal testing machine (UTM) equipped with a 2.5 kN load cell, where the crosshead speed was set to 2.5 mm min^{-1} [18].

Uniaxial compression tests were performed on prismatic 3D printed bulk samples (width = 12.7 mm, depth = 12.7 mm, height = 25.4 mm) using an MTS UTM equipped with a 300 kN load cell. These tests were performed at a crosshead speed of 3 mm min^{-1} according to ASTM D695. The same crosshead speed was used to perform in-plane and out-of-plane compression tests on the 3D printed honeycomb structures where optical images were recorded during the tests using a Nikon D5300 DSLR camera to observe the deformation mechanisms and failure modes of the cellular structures.

During the mechanical tests, the average *piezoresistive response* of the nanocomposite samples was measured *in situ* by recording the change in the electrical resistance of the samples, ΔR, using a DMM 4050 multimeter (Tektronix, USA). To limit the contact resistance, a layer of copper foil was placed between the sample and the alligator clips of the multimeter, as shown in Fig. S8 (Supplementary Material). Note that the loading train of the UTM was insulated via an insulating adhesive tape. For the compression tests, the top and bottom surfaces of the samples were ground prior to testing to guarantee a fully conforming contact with the copper foil. This was necessary to minimize the effect of the applied stress on the contact resistance. Furthermore, a slight pre load (~5 N) was applied to ensure that the sample was in firm contact with the electrodes throughout the test. The measured ΔR values were synchronized with the strain readings, ε, of the UTM, and the obtained data was used to calculate the gauge factor in the elastic regime:

$$GF = \frac{\Delta(\Delta R/R_0)}{\Delta\varepsilon} \quad (2)$$

The gauge factor represents the average slope of the $\Delta R/R_0$ vs. ε curve over a chosen strain interval $\Delta\varepsilon$. Here, R_0 represents the initial resistance of the samples at zero load. It is important to note that at least three samples were tested for every case described above, and the average values along with the corresponding error bars (standard deviation) are reported in the following section.

3. Results and discussion

3.1. Morphological and thermal characteristics

In Fig. S3 (Supplementary Material), we present SEM images of the MWCNT/PA12 powder feedstocks, showing nearly spherical particles after ball milling, similar to the particle morphology observed in the as-received PA12 powders (see Fig. S2a, Supplementary Material). The SEM images (Fig. S3, Supplementary Material) also show the presence of MWCNTs on the surface of the PA particles which appear to be well-dispersed, particularly for the case of PA-0.3. However, large agglomerates of MWCNTs are observed in the SEM images of the PA-1 powder, which resemble the morphology of the as-received MWCNTs (see Fig. S2b, Supplementary Material).

Fig. 2 shows the DSC thermograms of pure PA12 and MWCNT/PA12 nanocomposite powders for (a) heating and (b) cooling cycles, respectively, while Table 1 summarizes the results obtained from the data analysis of the respective DSC thermograms. We observe a decrease in the melting temperature, T_m, and an increase in the crystallization temperature, T_c, with the addition of MWCNTs in line with previous study [34]. The latter decrease in T_m can be attributed to the higher heat conductance of the MWCNT network [34], while the observed increase in T_c is explained by the fact that MWCNTs act as nucleation sites, facilitating the crystallization of the polymer matrix [34,43]. With the addition of MWCNTs, we also observe broadening of the melting peaks (see Fig. 2) which, in turn, promotes undesired sintering of the non-laser irradiated powder particles and therefore renders the SLS process more challenging [28]. In general, the addition of MWCNTs increased the crystallinity relative to the pure PA12 powder (PA-0) (see, Table 1) in Supplementary Material). However, the maximum increase in X of ~6% was observed for the composite powder with 0.5 wt% MWCNT loading; at higher concentrations of MWCNT, the crystallinity dropped slightly which can be attributed to the presence of agglomerated MWCNT bundles that act as impurities and hamper the alignment of polymer chains during the crystallization process [44].

In Fig. 3a and b, we present the TGA and DTG thermograms of pure MWCNTs, pure PA12 and MWCNT/PA12 nanocomposites.

Table 1 – Summary of DSC and TGA data for pure PA12 and MWCNT/PA12 nanocomposites: T_m is the melting temperature, T_{mo} is onset melting temperature, T_c is crystallization temperature, T_{co} is onset crystallization temperature, ΔH_m is melting enthalpy, X is crystallinity (%), T_d is thermal degradation temperature, and WL is weight loss (%).

Sample ID	T_m (°C)	T_{mo} (°C)	T_c (°C)	T_{co} (°C)	ΔH_m (J/g)	X (%)	T_d (°C)	WL (%)
PA-0	184	173	153	160.5	85	40.7	450	98.7
PA-0.3	182	171	155.5	160	86.4	41.3	451.5	98.4
PA-0.5	181	169.4	156	163	90	43.1	452	98.1
PA-1	179	168.6	157	164	79.3	37.9	453	97.7

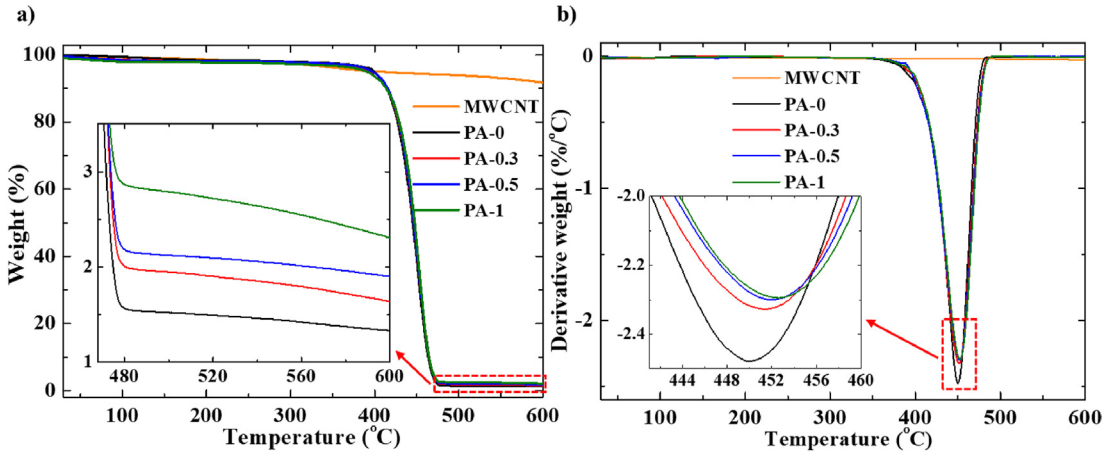

Fig. 3 – (a) TGA (b) DTG thermograms of pure MWCNTs, pure PA12 and MWCNT/PA12 nanocomposites. Insets are zoomed-in portion of the plots indicated by the dashed rectangle.

These thermograms show slightly higher thermal degradation temperatures, T_d, and lower weight losses (*WL* in %) of the samples with increasing MWCNT loading (see Table 1 for numerical values of T_d and *WL*). Since the carbonaceous nano-fillers possess high thermal stability, their addition to the polymer matrix delays the thermal degradation of the composite, as reported in previous studies [45–47]. The enhancement in thermal stability can also be ascribed to the fact that the MWCNT network in the polymer matrix acts as a mass transfer barrier, thus decreasing the degradation of the composite by hampering the movement of polymeric chains at elevated temperatures [48].

3.2. *Mechanical and piezoresistive behavior of bulk nanocomposites*

As seen from the tensile stress-strain responses shown in Fig. 4a, the 3D printed MWCNT/PA12 samples showed a

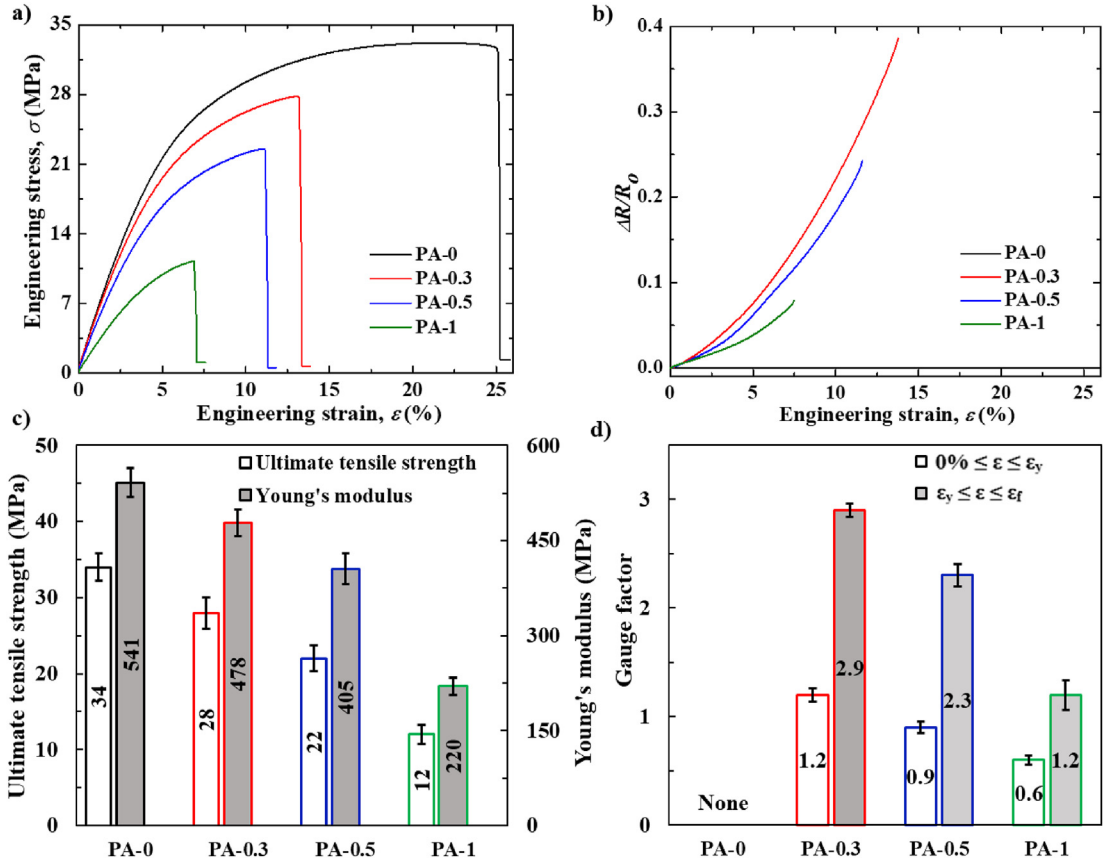

Fig. 4 – (a) Engineering stress-strain response, (b) piezoresistive response (c) mechanical properties, and (d) gauge factors of pure PA12 and MWCNT/PA12 nanocomposites under uniaxial monotonic tensile loading.

decrease in the ultimate tensile strength, Young's modulus and elongation at break with increasing MWCNT content. Specifically, the addition of 1 wt% MWCNT resulted in a ≈60% reduction in Young's modulus (taken as the secant modulus at the yield strain, ε_y) and tensile strength (see Fig. 4c), as compared to the neat PA12. Note that these trends are similar to those observed in three-point bending experiments (presented in Section S3, Supplementary Material). This can be attributed to the lower bed temperatures used to print nanocomposite samples (as discussed in Section 2.3) which resulted in a higher porosity in printed samples, as confirmed via SEM (see Fig. 5) and μ-CT images (see Fig. S4, Supplementary Material). Moreover, large agglomerates of MWCNTs weakened the interfacial bonding between nanotubes and the matrix as observed from the SEM images of the samples with higher concentration of MWCNTs (see Fig. 5). Furthermore, the sample with the lowest MWCNT concentration (PA-0.3) was found to be the most sensitive in terms of the piezoresistive sensitivity (see Fig. 4c) in the elastic ($0 \leq \varepsilon \leq \varepsilon_y$) and inelastic regime ($\varepsilon_y \leq \varepsilon \leq \varepsilon_f$ where ε_f is the fracture strain) as compared to those of nanocomposites with higher MWCNT loading (see Fig. 4d). The yield strain, ε_y, represents a point on the stress-strain curve from where unloading to zero stress would yield a permanent strain of 0.1% [49]. Note that the same trend in sensitivity values with respect to the wt.% of MWCNT was also observed in three-point bending tests (see Section S3, Supplementary Material). In the samples with lower MWCNT content (i.e. PA-0.3), the number of conductive channels in the percolating network is lower and the average distance between the MWCNTs is larger. This increases the probability of breaking the transfer of electrons in a conductive channel under tensile straining, which, in turn, yields a

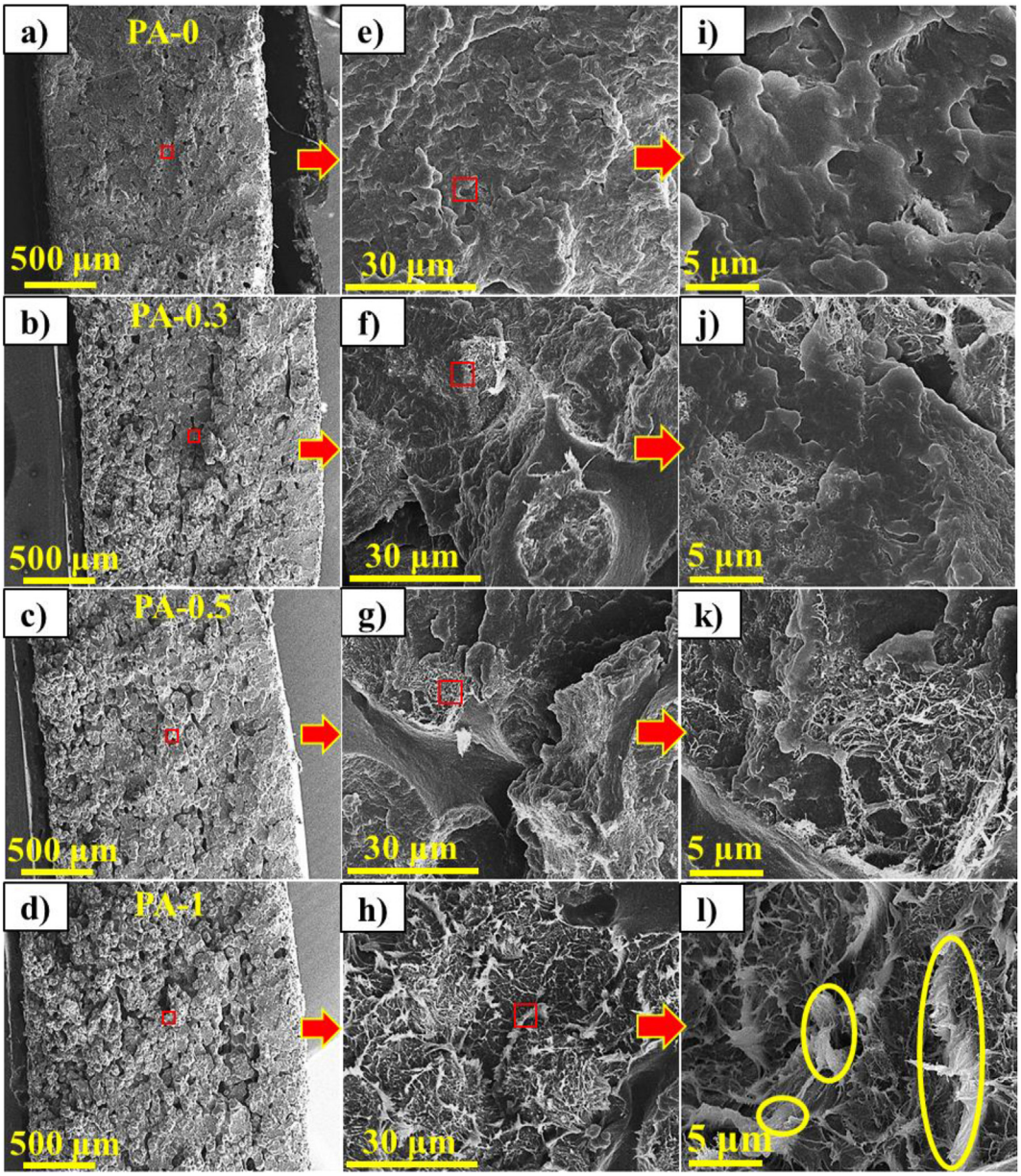

Fig. 5 – SEM images of fracture surfaces at various magnifications: (a) pure PA12; (b)–(d) MWCNT/PA12 nanocomposites.

higher piezoresistive sensitivity Note that the limits of normalized resistance change are 0 and ∞ (i.e. $\Delta R/R_0 = [0, \infty]$) under tension/flexural loading, according to Eq. (2). Moreover, the electrical conductivity of the 3D printed nanocomposites across the gauge section of the dogbone samples at zero load ranged between 2 and 286 S cm^{-1} (see Fig. S9, Supplementary Material) with a percolation threshold that lies between 0.2 and 0.3 wt% of MWCNT. It is to be noted that the percolation threshold depends on various factors such as morphology, conductivity, and dispersion state of the fillers within the polymer matrix along with the morphology of the polymer [2,50,51] apart from the concentration of conductive fillers.

Under uniaxial compression (see Fig. 6), the mechanical and piezoresistive properties showed similar trends as in uniaxial tension. However, the deterioration of mechanical properties (Young's modulus, yield strength) with increasing MWCNT loading (see Fig. 6b) was less pronounced, because the porous structure tends to densify and the defects are less likely to grow under compressive loading as compared to tensile loading.

Furthermore, the nanocomposites exhibited excellent piezoresistive sensitivity under compressive loading in the elastic regime (see Fig. 6c), reporting an initial gauge factor (*GF*) of 31 for the PA-0.3 sample (see Fig. 6d), which is 25 times the gauge factor measured under uniaxial tension ($GF = 1.2$). Note that the limits of normalized resistance change are 0 and -1 (i.e. $-\Delta R/R_0 = [0, 1]$) under compression, according to Eq. (2). It is worth mentioning that the gauge factor of the PA-0.3 sample under uniaxial compression ($GF = 31$) is higher than those reported for extant piezoresistive self-sensing composites, which typically show gauge factors in the range of 1–28 [52]. We hypothesize that the porosity in our 3D printed MWCNT/PA12 composites played a crucial role in enhancing the piezoresistive sensitivity. It is reasonable to expect that loosely connected MWCNTs on the surfaces of internal pores would eventually come in contact and form additional conductive channels under compressive loading. This hypothesis is affirmed by the results obtained from *in situ* μ-CT scans, which show noticeable densification and disappearance of smaller pores, in the 3D printed sample over a compressive strain range of 10%, as seen from Fig. 7 (see also Fig. S5, Supplementary Material). Beyond the yield point, however, the relative resistance change, $\Delta R/R_0$, remains almost constant throughout the inelastic regime, as seen from Fig. 6c, indicating that the inelastic deformation or damage progression rate in this regime is constant.

3.3. *Piezoresistive and mechanical behavior of hexagonal honeycomb composite structures*

Having examined the mechanical and piezoresistive characteristics of the 3D printed MWCNT/PA12 bulk nanocomposites, we now demonstrate that these composites can be effectively used to build self-sensing lightweight structures

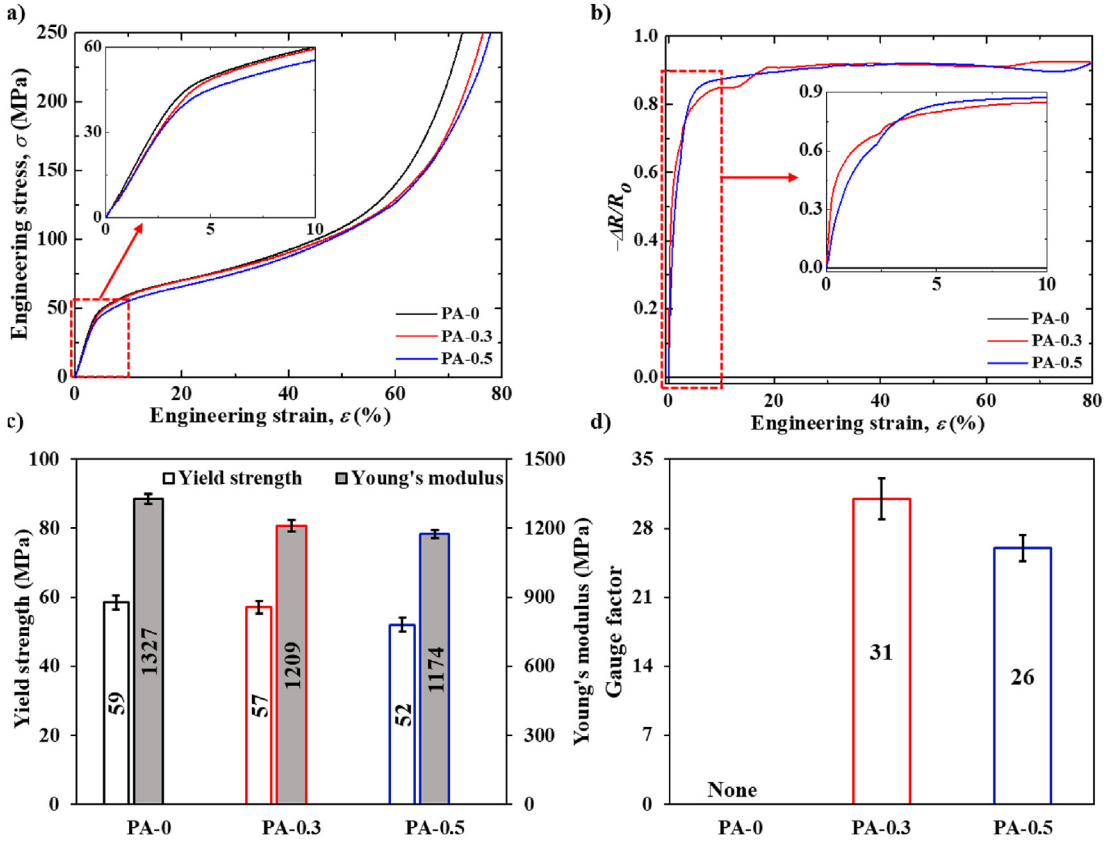

Fig. 6 – (a) Engineering stress-strain response, (b) mechanical properties, (c) piezoresistive response and (d) gauge factors (calculated in strain range of 0% ≤ ε ≤ ε_y) of pure PA12 and MWCNT/PA12 nanocomposites (bulk samples) under uniaxial compression. Insets are zoomed portions of the plots, as indicated by the dashed boxes.

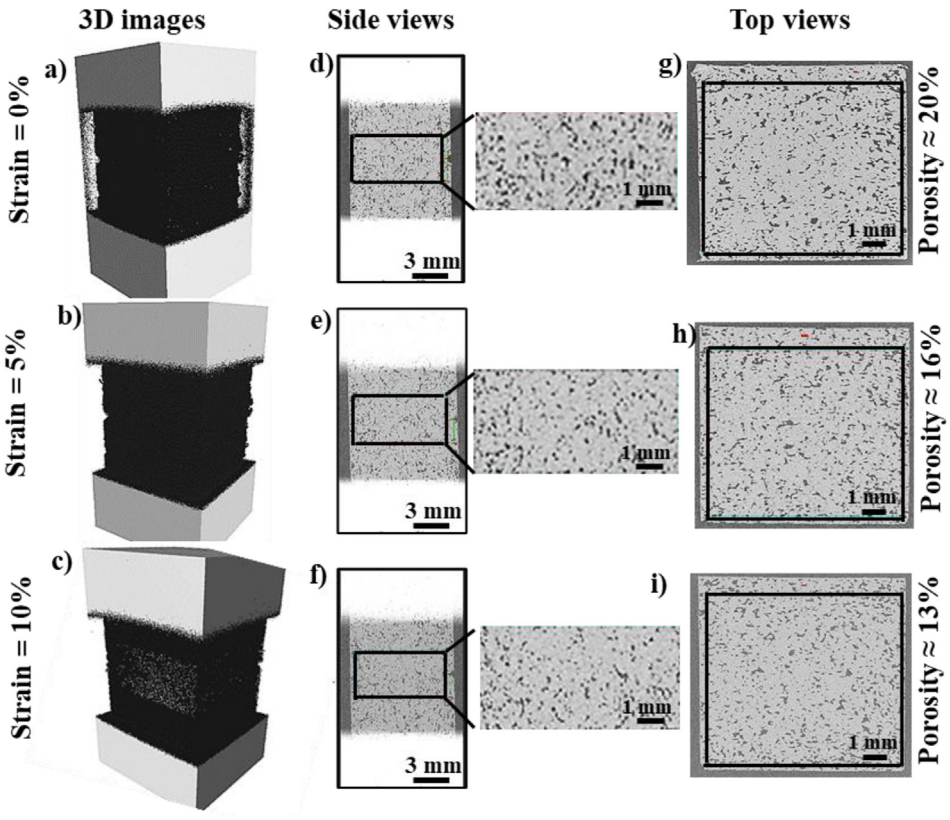

Fig. 7 – μ-CT images captured *in situ* under uniaxial compression of a prismatic MWCNT/PA12 nanocomposite sample with 0.3 wt% MWCNT loading (PA-0.3) up to a strain of 10%.

via SLS additive manufacturing. To this end, we examine, in this section, the mechanical and piezoresistive responses of MWCNT/PA12 hexagonal honeycomb composite structures subject to in-plane and out-of-plane compression. To evaluate the effect of parent material of cellular structures with a relative density of 40%, three different compositions (PA-0, PA-0.3 and PA-0.5) were examined.

3.3.1. *In-plane response*

Fig. 8a and b shows the in-plane mechanical and piezoresistive responses of hexagonal honeycomb structures made from neat PA12 and MWCNT/PA12, respectively, along with the corresponding deformation maps (see Fig. 8c) recorded during the compression tests. Note that the stress presented in Fig. 8a is the average engineering stress induced in the lattice structure and was calculated by dividing the applied force with the effective cross-sectional area (26×17 mm^2 for in-plane loading, and 26×26 mm^2 for out-of-plane loading). The measured stress-strain responses (Fig. 8a) can be divided into three stages: 1) an initial linear elastic regime (prior to point A); 2) a stress plateau with superimposed stress fluctuations representing the collapse response of the cellular structure (between points A and B); 3) a densification stage in which the fully collapsed cellular structure is further compressed (following point B). For all three samples, structural collapse occurs through the formation of plastic hinges at the nodal points (see Fig. 8c). Once the cell walls of the honeycomb come into contact (at frame B in Fig. 8c), the load is transferred more effectively across and through the cell walls and this gives rise to pronounced strain hardening, signifying the onset of densification. For the structure with the highest MWCNT loading (PA-0.5), we observe partial fragmentation in the top left corner at the onset of collapse (see frame A in Fig. 8c). This is explained by the fact that the embedded MWCNTs restrict the movement of polymeric chains, and thus reduce the failure strain of the composite, as reported in Section 3.2. The piezoresistive responses observed for the PA-0.3 and PA-0.5 honeycomb structures (see Fig. 8b) showed similar attributes as those observed for the corresponding bulk samples under uniaxial compression. However, an average increase in the $\Delta R/R_0$ trend is observed in Fig. 8b (see **videos SV1-3**, Supplementary Material), although $\Delta R/R_0$ fluctuates during the collapse of the cellular structures due to the formation of crush bands, resulting in simultaneous breakage and formation of conductive paths in the honeycomb structure. Following the onset of densification, percolation of contacts occurs due to folds formed between cell walls in the honeycomb structure, leading to the formation of additional conductive paths, yielding a steady drop in the resistance $\Delta R/R_0$ with increasing deformation. At a compressive strain of $\approx$60%, the honeycomb structures are densified to the point where the initial electrical resistance is almost fully lost, reporting $\Delta R/R_0 \approx -1$ (see Fig. 8b). It is interesting to note that the gauge factors of the PA-0.3 and PA-0.5 honeycomb structures (see inset of Fig. 8b) are lower than those measured in uniaxial compression which can be attributed to two factors:

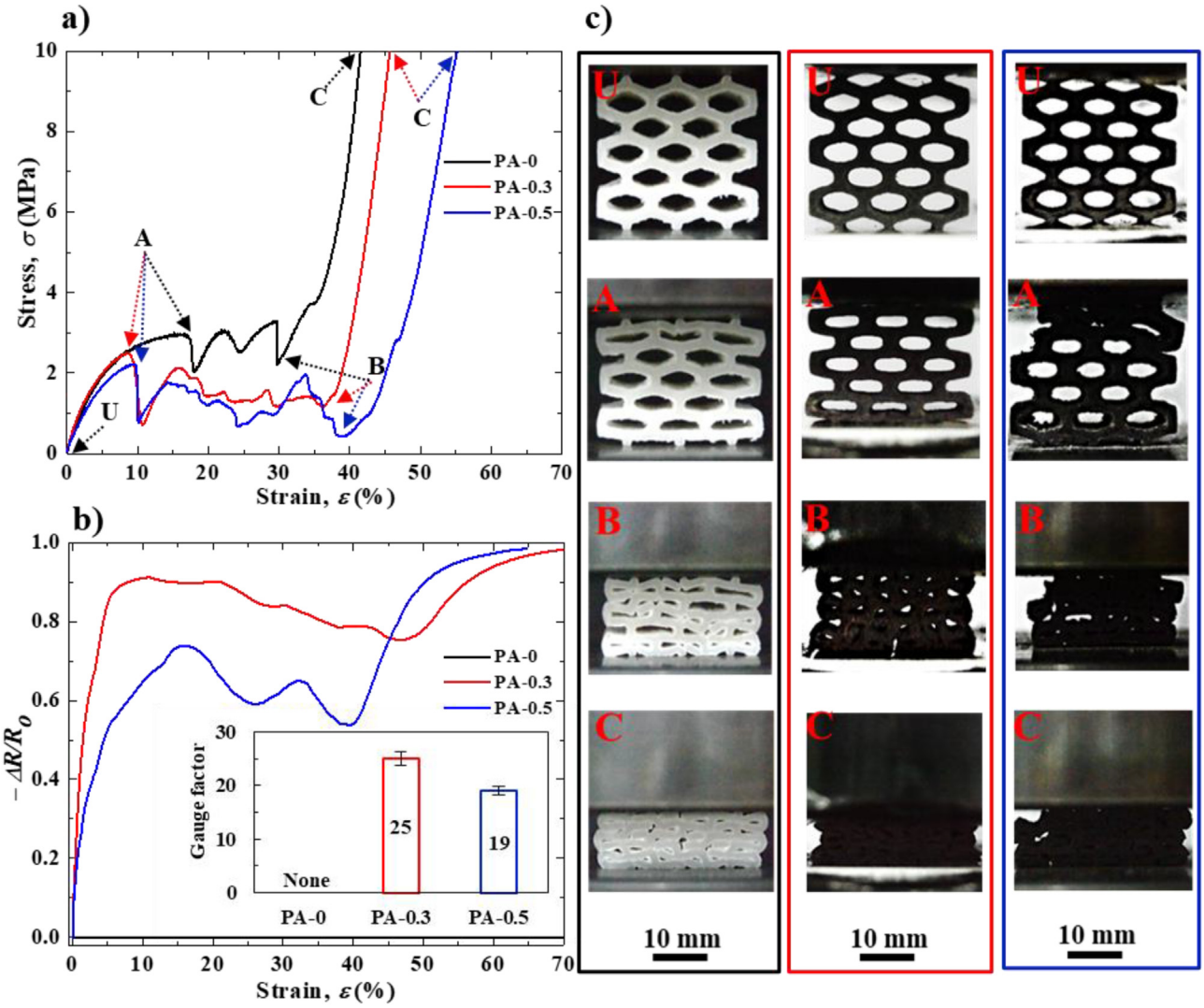

Fig. 8 – (a) Effective stress-strain response, (b) piezoresistive response and (c) deformation maps at various stages of the response for pure PA12 and MWCNT/PA12 nanocomposites (hexagonal structure with 40% relative density) under uniaxial compression (in-plane). Inset of (b): comparison of gauge factors (evaluated in elastic regime). Note that the alphabets used in (a) represents the following points on the curves corresponding to deformation maps in (c): U = Unloaded, A = Initial collapse stress, B = Densification onset, C = Densification.

(i) the occurrence of a combination of compressive and bending stresses in the cell walls due to the bend-dominated nature of the hexagonal honeycombs under in-plane loading, and (ii) the presence of a non-conductive medium (i.e. air) within the honeycomb cells, which elevates the zero load resistance of the effective medium, R_0, and therefore decreases its gauge factor.

Supplementary video related to this article can be found at https://doi.org/10.1016/j.jmrt.2023.08.051

Based on the stress-strain curves shown in Fig. 8a, we evaluated the initial collapse stress, the elastic modulus, the densification strain, and the specific energy absorption (SEA) of all cellular structures considered herein and plotted the results in Fig. S10 (Supplementary Material). Here, we define the densification strain, ε_d, as the strain at which the stress reaches a value of 10 MPa for all cellular structures, corresponding to point C in Fig. 8a. The SEA was calculated as follows [53]:

$$SEA = \frac{1}{\rho}\int_0^{\varepsilon_d} \sigma d\varepsilon \tag{3}$$

where ρ represents the average density of the lattice structure. As seen from Figs. S10a and b (Supplementary Material), both the (in-plane) collapse strength and elastic modulus of the honeycomb structures decrease steadily with increasing MWCNT content, in line with the results obtained for the bulk samples (see Section 3.2). While the densification strain is observed to increase with increasing wt.% MWCNT (see Fig. S10c, Supplementary Material), due to more pronounced fragmentation of the brittle cell walls at higher MWCNT

loading, the SEA is seen to decrease (see Fig. S10d) which is attributed to the decrease in collapse strength and the loss of ductility with the addition of MWCNTs.

3.3.2. *Out-of-plane response*

In Fig. 9a and b, we present the mechanical and piezoresistive responses of PA12 and MWCNT/PA12 honeycomb structures subject to out-of-plane compression, including the corresponding deformation maps (see Fig. 9c). Since the relative density of honeycomb structure tested is high (40%), we observe collapse of the honeycomb structures triggered by a global buckling mechanism as reported elsewhere [36]. Note that the collapse commences at point A (see Fig. 9c and **videos SV4-6** in the Supplementary Material) and causes a significant load drop, as seen from Fig. 9a. Subsequently, the cell walls fold and come into contact as the deformation increases, ultimately resulting in densification of the cellular structures with pronounced strain hardening (Fig. 9a). The cell walls of the PA-0.3 and PA-0.5 honeycombs show signs of cracking during the post-buckling response (see Fig. 9c), due to the brittle nature of the MWCNT/PA12 nanocomposites. The corresponding out-of-plane mechanical properties are plotted separately in Fig. S11 (Supplementary Material), for comparison, noting that the densification strains reported in Fig. S11c (Supplementary Material) were evaluated as the strains at which the stresses reached 25 MPa for all cellular structures (points C in Fig. 9a). Since the deformation of the honeycomb is fully stretch-dominated under out-of-plane compression (prior to the onset of buckling), the elastic modulus (see Fig. S11b, Supplementary Material), collapse strength (see Fig. S11a, Supplementary Material) and SEA (see Fig. S11d, Supplementary Material) are considerably higher than those observed under in-plane compression, as expected. However, the out-of-plane mechanical properties (see Fig. S11, Supplementary Material) degrade with increasing MWCNT content in a similar way as observed for the case of in-plane compression (see Fig. S10, Supplementary Material).

Supplementary video related to this article can be found at https://doi.org/10.1016/j.jmrt.2023.08.051

As shown in Fig. 9b, the out-of-plane piezoresistive responses of the PA-0.3 and PA-0.5 honeycomb composite

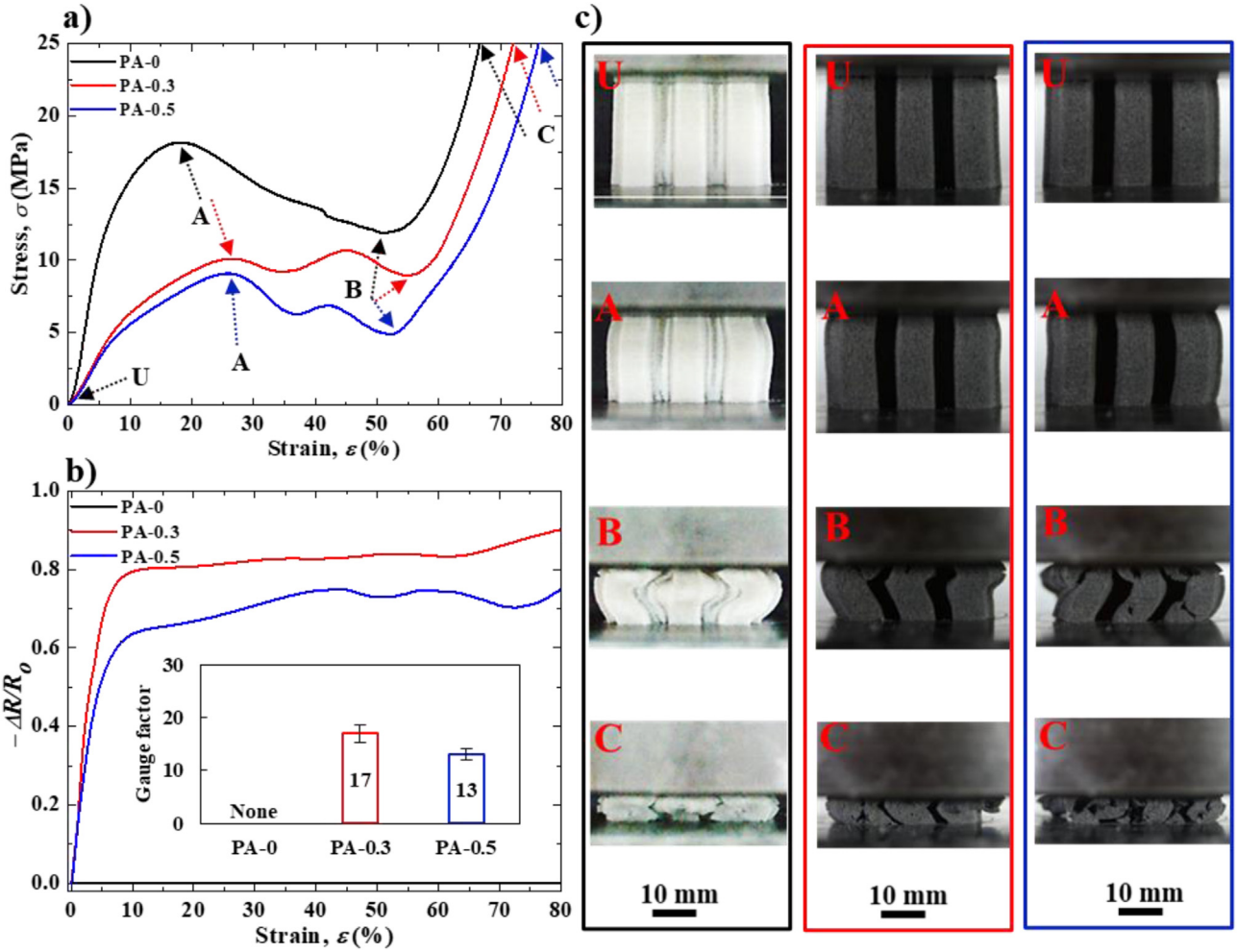

Fig. 9 – (a) Effective stress-strain response (b) Piezoresistive response and (c) Deformation maps at various stages of the response for pure PA and MWCNT/PA nanocomposites (hexagonal structure with 40% relative density) under uniaxial compression (out-of-plane). Inset of (b): comparison of gauge factors (elastic regime). Note that the alphabets used in (a) represents the following points on curves corresponding to deformation maps in (c): U = Unloaded, A = Initial collapse stress, B = Densification onset, C = Densification.

structures show similar characteristics and initial gauge factors (see inset) as those observed for in-plane compression (Fig. 8b). However, the $\Delta R/R_0$ curve only shows minor fluctuations during the out-of-plane collapse response (Fig. 9b) due to the absence of crush bands. It is also observed that $\Delta R/R_0$ does not approach the limiting value of -1 which can be attributed to the more pronounced lateral expansion of the sample under out-of-plane compression, limiting the rate of densification.

It is to be noted that the gauge factors of the MWCNT/PA12 honeycomb structures in the inelastic regime (also known as damage sensitivity) are lower than those measured in the elastic regime (also known as strain sensitivity) under both in-plane and out-of-plane compression. The evolution of piezoresistance in the densification regime is principally controlled by the percolation of contacts between cell walls along with other inelastic processes (i.e. plasticity and microscopic damage of cell walls). Here, we define the damage sensitivity as follows:

$$GF = \frac{\Delta R/R_0}{\varepsilon_d - \varepsilon_y} \tag{4}$$

where ε_d is the densification strain as discussed above for in-plane and out-of-plane compression of honeycomb structures (see sections 3.3.1 and 3.3.2) and ε_y is the initial yield strain. The gauge factors in the inelastic regime are summarized in Table S2 (Supplementary Material).

4. Conclusions

In this study, we examined the piezoresistive and mechanical behavior of bulk and cellular MWCNT/PA12 composites fabricated via selective laser sintering (SLS). Following an optimization of the SLS processing parameters, we 3D printed standard test specimens for tensile, compressive and flexural testing, as well as hexagonal honeycomb structures (40% relative density) whose mechanical and piezoresistive responses were measured under both in-plane and out-of-plane compression.

It was found that the 3D printed MWCNT/PA12 composites had a lower strength and stiffness than the neat PA12, particularly under tensile loading, which was mainly attributable to the increase in porosity with increasing MWCNT loading. The influence of porosity on mechanical properties was found to be more dominant than that of the reinforcing effect of MWCNTs and crystallinity increase due to the addition of MWCNTs. Under uniaxial compression, the nanocomposites showed significantly less deterioration in the mechanical properties due to densification of the sintered samples under compressive loading, as confirmed by *in situ* μ-CT images. The piezoresistive measurements showed that the 3D printed MWCNT/PA12 composite with the lowest MWCNT loading (0.3 wt%) revealed the highest (initial) gauge factors, reporting 1.2 and 31 for uniaxial tension and compression, respectively. The exceptionally high gauge factor of 31 was attributed to the densification of the porous MWCNT/PA12 microstructure, forming additional conductive networks under compressive loading, The in-plane compressive response of the MWCNT/PA12 honeycomb structures was accompanied by the formation of plastic hinges combined with partial fracture of cell walls, while under out-of-plane compression, their structural collapse was triggered by global buckling of honeycomb cells. For both in-plane and out-of-plane loading, the ductility of the 3D printed MWCNT/PA12 was sufficient to observe a distinct stress plateau as well as full densification of the cellular structure. It was also demonstrated, that the MWCNT/PA12 honeycombs possess excellent strain sensing functionalities, reporting gauge factors up to 25 and 17 for in-plane and out-of-plane loading, respectively. These results suggest that SLS 3D printing is a suitable technique for fabricating mechanically robust lightweight structures with exceptional *in situ* strain and damage sensing capabilities.

Declaration of competing interest

The authors declare that they have no known competing financial interests or personal relationships that could have appeared to influence the work reported in this paper.

Acknowledgements

The authors would like to acknowledge the funding provided by Khalifa University through the Competitive Internal Research Award (CIRA) [grant number: CIRA-2018-128]. The authors would like to thank Mr. P. George from the Advanced Research and Innovation Center (ARIC) at Khalifa University for assisting with the μ-CT scans.

Appendix A. Supplementary data

Supplementary data to this article can be found online at https://doi.org/10.1016/j.jmrt.2023.08.051.

REFERENCES

[1] Verma P, Schiffer A, Kumar S. Thermo-resistive and thermo-piezoresistive sensitivity of carbon nanostructure engineered thermoplastic composites processed via additive manufacturing. Polym Test 2021;93:106961.
[2] Kumar S, Gupta TK, Varadarajan KM. Strong, stretchable and ultrasensitive MWCNT/TPU nanocomposites for piezoresistive strain sensing. Composites Part B 2019;177:107285.
[3] Arif MF, Alhashmi H, Varadarajan KM, Koo JH, Hart AJ, Kumar S. Multifunctional performance of carbon nanotubes and graphene nanoplatelets reinforced PEEK composites enabled via FFF additive manufacturing. Composites Part B 2020;184:107625.
[4] Kumar S, Dhawan R, Shukla SK. Flame retardant polymer nanocomposites: an overview. Macromol Symp 2023;407:1–11.
[5] Guo J, Song H, Liu H, Luo C, Ren Y, Ding T, et al. Polypyrrole-interface-functionalized nano-magnetite epoxy nanocomposites as electromagnetic wave absorbers with enhanced flame retardancy. J Mater Chem C 2017;5:5334–44.
[6] Azam MU, Samad MA. UHMWPE hybrid nanocomposite coating reinforced with nanoclay and carbon nanotubes for tribological applications under water with/without abrasives. Tribol Int 2018;124:145–55.

[7] Sun K, Fan R, Zhang X, Zhang Z, Shi Z, Wang N, et al. An overview of metamaterials and their achievements in wireless power transfer. J Mater Chem C 2018;6:2925–43.
[8] Hu Z, Shao Q, Huang Y, Yu L, Zhang D, Xu X, et al. Light triggered interfacial damage self-healing of poly(p-phenylene benzobisoxazole) fiber composites. Nanotechnology 2018;29.
[9] Guo N, Leu MC. Additive manufacturing: technology, applications and research needs. Front Mech Eng 2013;8:215–43.
[10] Raimondo M, Guadagno L, Speranza V, Bonnaud L, Dubois P, Lafdi K. Multifunctional graphene/POSS epoxy resin tailored for aircraft lightning strike protection. Composites Part B 2018;140:44–56.
[11] Naebe M, Abolhasani MM, Khayyam H, Amini A, Fox B. Crack damage in polymers and composites: a review. Polym Rev 2016;56:31–69.
[12] Nauman S. Piezoresistive sensing approaches for structural health monitoring of polymer composites—a review. Eng 2021;2:197–226.
[13] Bekas DG, Hou Y, Liu Y, Panesar A. 3D printing to enable multifunctionality in polymer-based composites: a review. Composites Part B 2019;179:107540.
[14] Andrew JJ, Alhashmi H, Schiffer A, Kumar S, Deshpande VS. Energy absorption and self-sensing performance of 3D printed CF/PEEK cellular composites. Mater Des 2021;208:109863.
[15] Verma P, Ubaid J, Varadarajan KM, Wardle BL, Kumar S. Synthesis and characterization of carbon nanotube-doped thermoplastic nanocomposites for the additive manufacturing of self-sensing piezoresistive materials. ACS Appl Mater Interfaces 2022;14:8361–72.
[16] Poompiew N, Pattananuwat P, Aumnate C, Román AJ, Osswald TA, Potiyaraj P. 3D printable resin/carbon nanotube composites for wearable strain sensors: enhancing mechanical and electrical properties. J Sci Adv Mater Devices 2023:8.
[17] Hernandez JA, Maynard C, Gonzalez D, Viz M, O'Brien C, Garcia J, et al. The development and characterization of carbon nanofiber/polylactic acid filament for additively manufactured piezoresistive sensors. Addit Manuf 2022;58:102948.
[18] Schneider J, Kumar S. Multiscale characterization and constitutive parameters identification of polyamide (PA12) processed via selective laser sintering. Polym Test 2020;86:106357.
[19] Han W, Kong L, Xu M. Advances in selective laser sintering of polymers. Int J Extrem Manuf 2022;4.
[20] Sivadas BO, Ashcroft I, Khlobystov AN, Goodridge RD. Laser sintering of polymer nanocomposites. Adv Ind Eng Polym Res 2021;4:277–300.
[21] Goodridge RD, Shofner ML, Hague RJM, McClelland M, Schlea MR, Johnson RB, et al. Processing of a Polyamide-12/carbon nanofibre composite by laser sintering. Polym Test 2011;30:94–100.
[22] Bain ED, Garboczi EJ, Seppala JE, Parker TC, Migler KB. AMB2018-04: benchmark physical property measurements for powder bed fusion additive manufacturing of polyamide 12. Integr Mater Manuf Innov 2019;8:335–61.
[23] Schmid M. Laser Sintering with Plastics: Technology, Processes, and Materials. Munich: Hanser Publishers; 2018.
[24] Tan LJ, Zhu W, Zhou K. Recent progress on polymer materials for additive manufacturing. Adv Funct Mater 2020:30.
[25] Technical Data sheet adsint PA12, BASF, Germany (www.basf.com).
[26] Chung H. Processing and Properties of Functionally Graded Polymer Composites Produced by Selective Laser Sintering. PhD thesis. The University of Michigan; 2005.
[27] Caulfield B, McHugh PE, Lohfeld S. Dependence of mechanical properties of polyamide components on build parameters in the SLS process. J Mater Process Technol 2007;182:477–88.
[28] Schmid M, Kleijnen R, Vetterli M, Wegener K. Influence of the origin of polyamide 12 powder on the laser sintering process and laser sintered parts. Appl Sci 2017;7.
[29] Moeskops E, Kamperman N, Van de Vorst B, Knoppers R. Creep behaviour of polyamide in selective laser sintering. In: Proc. 15th solid free. Fabr. Symp. Texas, USA: University of Texas in Austin; 2004. p. 60–7.
[30] Athreya SR, Kalaitzidou K, Das S. Processing and characterization of a carbon black-filled electrically conductive Nylon-12 nanocomposite produced by selective laser sintering. Mater Sci Eng A 2010;527:2637–42.
[31] Yuan S, Zheng Y, Chua CK, Yan Q, Zhou K. Electrical and thermal conductivities of MWCNT/polymer composites fabricated by selective laser sintering. Compos Part A Appl Sci Manuf 2018;105:203–13.
[32] Xiong Y, Pei H, Lv Q, Chen Y. A facile fabrication of PA12/CNTs nanocomposites with enhanced three-dimensional segregated conductive networks and electromagnetic interference shielding property through selective laser sintering. ACS Omega 2022;7:4293–304.
[33] Ji M, Deng H, Yan D, Li X, Duan L, Fu Q. Selective localization of multi-walled carbon nanotubes in thermoplastic elastomer blends: an effective method for tunable resistivity-strain sensing behavior. Compos Sci Technol 2014;92:16–26.
[34] Yuan S, Bai J, Chua CK, Wei J, Zhou K. Material evaluation and process optimization of CNT-coated polymer powders for selective laser sintering. Polymers 2016;8:1–17.
[35] Zhou M, Zhu W, Yu S, Tian Y, Zhou K. Selective laser sintering of carbon nanotube–coated thermoplastic polyurethane: mechanical, electrical, and piezoresistive properties. Compos Part C Open Access 2022;7:100212.
[36] Kumar S, Ubaid J, Abishera R, Schiffer A, Deshpande VS. Tunable energy absorption characteristics of architected honeycombs enabled via additive manufacturing. ACS Appl Mater Interfaces 2019;11:42549–60.
[37] Saadi OW, Schiffer A, Kumar S. Piezoresistive behavior of DLP 3D printed CNT/polymer nanocomposites under monotonic and cyclic loading. Int J Adv Manuf Technol 2023:1965–78.
[38] Li ZY, Wang YZ, Ma TX, Zheng YF, Zhang C, Li FM. A self-sensing and self-actuating metamaterial sandwich structure for the low-frequency vibration mitigation and isolation. Compos Struct 2022;297:115894.
[39] Arif MF, Kumar S, Gupta TK, Varadarajan KM. Strong linear-piezoresistive-response of carbon nanostructures reinforced hyperelastic polymer nanocomposites. Compos Part A Appl Sci Manuf 2018;113:141–9.
[40] Yuan S, Chua CK, Zhou K. 3D-Printed mechanical metamaterials with high energy absorption. Adv Mater Technol 2019;4:1–9.
[41] Gogolewski S, Czerniawska K, Gasiorek M. Effect of annealing on thermal properties and crystalline structure of polyamides. Nylon 12 (polylaurolactam). Colloid Polym Sci 1980;258:1130–6.
[42] Maurer J, Jerabek M, Salaberger D, Thor M, Kastner J, Major Z. Stress relaxation behaviour of glass fibre reinforced thermoplastic composites and its application to the design of interrupted in situ tensile tests for investigations by X-ray computed tomography. Polym Test 2022:109.
[43] Bai J, Goodridge RD, Hague RJM, Song M. Improving the mechanical properties of laser-sintered polyamide 12 through incorporation of carbon nanotubes. Polym Eng Sci 2013;53:1937–46.
[44] Kurtz SM. UHMWPE Biomaterials Handbook. second ed. Boston: Academic Press; 2009.

[45] Yan C, Hao L, Xu L, Shi Y. Preparation, characterisation and processing of carbon fibre/polyamide-12 composites for selective laser sintering. Compos Sci Technol 2011;71:1834–41.
[46] Dorigato A, Brugnara M, Pegoretti A. Novel polyamide 12 based nanocomposites for industrial applications. J Polym Res 2017;24:1–13.
[47] Warnakula A, Singamneni S. Selective laser sintering of nano Al2O3 infused polyamide. Materials 2017;10.
[48] Yuan Y, Wu W, Hu H, Liu D, Shen H, Wang Z. The combination of Al2O3and BN for enhancing the thermal conductivity of PA12 composites prepared by selective laser sintering. RSC Adv 2021;11:1984–91.
[49] Henry C, Rupel K, Park C, Costanzo J, Kaczowka C. Evaluation of an alternate Method for Determining Yield Strength Offset Values for Selective Laser Sintered Polymeric Materials. SAMPE 2019 - Charlotte, NC; 2019.
[50] Avilés F, Oliva-Avilés AI, Cen-Puc M. Piezoresistivity, strain, and damage self-sensing of polymer composites filled with carbon nanostructures. Adv Eng Mater 2018;20:1–23.
[51] Mora A, Verma P, Kumar S. Electrical conductivity of CNT/polymer composites: 3D printing, measurements and modeling. Composites Part B 2020;183:107600.
[52] Verma Pawan, Ubaid Jabir, Alam Fahad, Suleyman Deveci SK. Multifunctional characteristics of 3D printed polymer nanocomposites under monotonic and cyclic compression. Def Technol 2023. https://doi.org/10.1016/j.dt.2023.05.017. In press.
[53] Thornton PH. Energy absorption in composite structures. J Compos Mater 1979;13:247–62.